Distance Measurement Using mmWave Radar: Micron Accuracy at Medium Range

Lukas Piotrowsky, *Graduate Student Member, IEEE*, Simon Kueppers, *Graduate Student Member, IEEE*, Timo Jaeschke, *Member, IEEE*, and Nils Pohl, *Senior Member, IEEE*

***Abstract*— This work provides a proof-of-concept for a linear-position sensor using an ultrawideband (UWB) frequency-modulated continuous wave (FMCW) radar system operating at 126–182 GHz. It is the first work to show environmental compensated and calibration-free distance measurements with micron accuracy at medium range using millimeter-wave (mmWave) radar technology. We addressed hardware imperfections, parameter estimation, and the free-space path, i.e., refractive index and near-field effects. The proposed signal processing chain is robust to interference and of low computational cost. Experiments reveal a systematic error of ± 1 μm over 4.8 m (0.8–5.6 m), and a random error at a minimum of 30 nm, providing very high sensitivity.**

***Index Terms*— Distance measurement, frequency-modulated continuous wave (FMCW) radar, linear position sensor, millimeter wave (mmWave) radar, near-field effects, radar theory, refractive index, signal processing, ultrawideband (UWB) radar.**

I. Introduction

INDUSTRIAL applications often require linear distance measurements for accurate positioning, motion control, machine calibration, or vibration monitoring [1]. Sophisticated sensing applications may demand accuracies on the order of micrometers at medium range, which is meters to tens of meters. Millimeter-wave (mmWave) technology (30–300 GHz) can meet the aforementioned criteria. It provides contact-free operation under harsh conditions with minimum maintenance.

Table I reviews relevant research on high-accuracy ranging using wideband and continuous wave (CW) radar technology. Table I reveals that most of the work is related to short-range metrology [2]–[11], which is in the range of millimeters to centimeters. These works primarily focus on hardware design [3]–[6], [8], [10]–[13], or just on precise parameter estimation [2]. However, distance measurement at medium range still raises questions about the free-space path, which is a systematic source of errors. As shown here, these errors can exceed the random error by three to four orders of magnitude, which may require calibration of the distance value [14].

Table I also shows a commercially available laser measurement system based on the Michelson interferometer, a well-established method for measuring the distance with very high accuracy. In contrast to Michelson interferometry, wideband radar can generally resolve multiple reflections and measure on an absolute scale.

This research is the first to show long-term reliable and calibration-free distance measurements with micron accuracy at medium range using a state-of-the-art ultrawideband (UWB) mmWave radar. We provide a proof-of-concept for a linear position sensor that has an accuracy comparable to optical instruments. This work addresses common sources of error, namely:

1) hardware imperfections;
2) inaccurate parameter estimation;
3) free-space path:
    a) speed of wave propagation in moist air;
    b) near-field effects.

In order to overcome these difficulties, we propose new techniques and discuss their technical and physical limitations.

Recent advances in European radio regulation will likely allow UWB mmWave radars to operate in the 116–260-GHz band from late 2022. Based on compatibility studies [15], a new regulation for a device class referred to as radiodetermination systems for industry automation in shielded environments (RDI-S), e.g., indoors, is currently under development [16]. In the United States, on the other hand, there is currently no regulation that allows operation in this frequency range in general. However, the Federal Communications Commission (FCC) permits a set of subbands for use by unlicensed devices [17].

In Section II, we begin with a description of the radar hardware and a signal model for the present application. Then in Section III, we propose some models describing the free-space path, and in Section IV, we propose a signal processing chain. Simulations and experimental results are discussed in Section V. Finally, we draw a conclusion in Section VI.

The Python code including several examples corresponding to the article is available online.[1]

Manuscript received 25 May 2022; revised 15 July 2022; accepted 21 July 2022. Date of publication 23 August 2022; date of current version 4 November 2022. This work was supported in part by the German Research Foundation (DFG) under Project 287022738—TRR 196 and in part by the Federal Ministry of Education and Research of Germany (BMBF) under Grant 16ME0179. *(Corresponding author: Lukas Piotrowsky.)*

Lukas Piotrowsky and Nils Pohl are with the Institute of Integrated Systems, Ruhr University Bochum, 44801 Bochum, Germany (e-mail: lukas.piotrowsky@rub.de).

Simon Kueppers and Timo Jaeschke are with 2π-Labs GmbH, 44801 Bochum, Germany.

Color versions of one or more figures in this article are available at https://doi.org/10.1109/TMTT.2022.3195235.

Digital Object Identifier 10.1109/TMTT.2022.3195235

[1] https://github.com/l-pio/mmwranging

TABLE I
OVERVIEW OF RELEVANT RESEARCH ON HIGH-ACCURACY RANGING USING RADAR TECHNOLOGY

Technology	Ctr. Frequency	Bandwidth	Scale	Accuracy	Range	Free-Space Path Model	Year / Ref.
laser interferometry[a]	$\lambda = 633\,\text{nm}$	-	incremental	$\pm 0.4\,\mu\text{m m}^{-1}$	0–30 m	refractive index	-
FMCW	10 GHz	2 GHz	absolute	±200 µm	5.1–5.25 m	not applied[b]	1997 / [2]
FSCW + CW	35 GHz	2 GHz	absolute	±100 µm	0.748–0.753 m	not applied[b]	1999 / [3]
FMCW	80 GHz	24.5 GHz	absolute	±350 µm	0–3 m	not applied	2012 / [12]
FMCW	80 GHz	25.6 GHz	absolute	±4 µm	0.725–0.775 m	not applied	2013 / [11]
six-port (two tone)	24 GHz	2.4 GHz	absolute	±200 µm	0–6 cm	not applied[b]	2013 / [4]
FMCW	146 GHz	48 GHz	absolute	±1 µm	0.65–0.66 m	not applied	2014 / [5]
FMCW	122.5 GHz	1 GHz	absolute	±2 µm	2–2.005 m	not applied[b]	2015 / [13]
				±200 µm	1–2.9 m		
FMCW + CW	59.5 GHz	5 GHz	absolute	±78 µm	0–5 mm	not applied[b]	2015 / [6]
FMCW	80 GHz	25 GHz	absolute	±15 µm	0–8 cm	not applied[b]	2017 / [7]
FMCW	124 GHz	6 GHz	absolute	±5 µm	1.6–1.635 m	not applied	2017 / [8]
six-port (CW)	24 GHz	-	incremental	±38 µm	0–15 cm	not applied[b]	2017 / [9]
FMCW	122 GHz	6.5 GHz	absolute	±10 µm	1.965–1.99 m	not applied[b]	2019 / [10]
FMCW	80 GHz	24 GHz	absolute	±4.5 µm	0.4–5.6 m	not applied (cal. required)	2019 / [14]
FMCW	154 GHz	56 GHz	absolute	±1 µm	0.8–5.6 m	refractive index + near-field correction	this work

[a] For the sake of comparison with optical metrology. Device: Lasertex HPI-3D.
[b] Or at least not mentioned in the publication.

TABLE II
PARAMETERS OF THE RADAR SENSOR

Parameter	Value
Manufacturer (model)	2π-Labs (2πSENSE) [18]
Type	PLL stabilized FMCW radar
Center frequency	154 GHz
Bandwidth	56 GHz[a] (36.4%)
Sweep duration	2 ms (500 Hz)
Phase noise	Less than −80 dBc/Hz @ 10 kHz
Sweep linearity	RMS frequency error: 600 kHz[b]
Reference oscillator	High precision TCXO, stability: ±100 ppb
Antenna	34.4 dBi[b] PTFE lens, HPBW: 2.7°[b]

[a] Range resolution: 3.9 mm (3-dB bandwidth, Hann window).
[b] Simulated value.

II. FMCW RADAR

A. Hardware

The monostatic radar hardware [18] was developed by 2π-Labs GmbH for versatile application in industry and science [19]. It is based on a homodyne frequency-modulated continuous wave (FMCW) architecture mainly radiating in the D-band. Table II lists the parameters and the configuration used here. The transceiver operates using triangular frequency modulation at a center frequency of 154 GHz with a bandwidth of 56 GHz, which corresponds to a range resolution of 3.9 mm. It uses an offset-phase-locked loop (PLL) concept [20], providing superior phase noise and sweep linearity at a very high bandwidth (see also [21], [22]). The antenna is a dielectric lens [23] with an aperture diameter of 36 mm, manufactured of polytetrafluoroethylene (PTFE). It has a particularly high gain of 34.4 dBi and a half-power beamwidth (HPBW) of 2.7° at the center frequency. Internally, the radar system uses a temperature-compensated reference oscillator with a stability of better than ±100 ppb over temperature. The developers paid close attention to the coherent and reproducible timing of the radio-frequency (RF) synthesizer and the analog-to-digital converter (ADC), which is of great importance for phase measurement [14].

B. Signal Model

Fig. 1 shows a block diagram of the signal model. A transmitter generates a frequency-modulated signal which is swept linearly over time, where the instantaneous frequency is

$$f_t = f_{\text{ctr}} + \dot{f}t, \quad -T/2 \le t \le T/2. \tag{1}$$

Here, t is termed as fast time, T is the sweep duration, f_{ctr} is the center frequency, and $\dot{f}$ is the sweep slope which is negative for downchirps. The transmit signal is radiated into free space, reflected at a radar target, and finally received back. The received signal is downconverted by using the transmit signal, i.e., the received signal is deramped, producing a signal at an intermediate frequency (IF) $\underline{s}_{\text{if}}(t)$. Generally, one can say that the FMCW radar system serves as a frequency-domain reflectometer [24], measuring the frequency response of the radar path $\underline{H}(f)$ as

$$\underline{s}_{\text{if}}(t) = \underline{H}(f_t) * \underline{h}_{\text{if}}(t). \tag{2}$$

In (2), $\underline{h}_{\text{if}}(t)$ is the impulse response of the receiver's IF path describing the IF-filter chain and timing discrepancies between the sampled data and the expected radio frequencies.

Assuming the radar path contains only a single target, then the frequency response is

$$\underline{H}(f) = A_\tau \exp(-\text{j}2\pi f \tau)\, \underline{H}_{\text{res},\tau}\, \underline{H}_{\text{nf},\tau}(f)\, \underline{H}_{\text{trx}}(f) \tag{3}$$

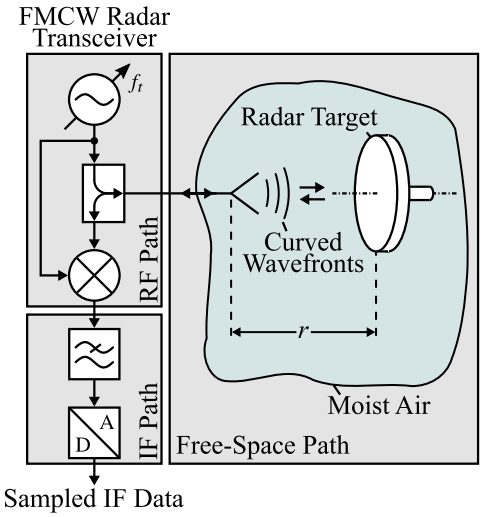

Fig. 1. Block diagram of the signal model.

where $A_\tau \exp(-\mathrm{j}2\pi f \tau)$ denotes the radio wave propagating through free space, τ is the time-of-flight (ToF, see Section III-A), and $\underline{H}_{\mathrm{trx}}(f)$ is the frequency response of the transceiver describing among other things dispersive waveguides and the variation of the transmitter's output power with frequency. Moreover,

$$\underline{H}_{\mathrm{res},\tau} = \exp(\mathrm{j}\pi \dot{f} \tau^2) \tag{4}$$

denotes a residual phase term appearing for frequency sweeps of a very steep slope [14], and

$$\underline{H}_{\mathrm{nf},\tau}(f) = \exp[-\mathrm{j}2\pi (f - f_{\mathrm{ctr}})\Delta\tau + \mathrm{j}\Delta\varphi] \tag{5}$$

accounts for the error introduced by far-field assumption [25] as investigated in Section III-B. Because of the particularly high range resolution, (3) neglects leakage, antenna mismatch, and multiple reflections as they are separable in the time domain [i.e., the radar echo $h(t)$]. Because of the very high antenna gain, multipath propagation is also neglected. The development of wideband quadrature mixers at mmWave frequencies is a challenging task that would drastically increase the hardware complexity. For that reason, the IF signal of the UWB mmWave radar is usually real-valued

$$s_{\mathrm{if}}(t) = \mathrm{Re}\{\underline{H}(f_t)\} \tag{6}$$

which can lead to erroneous distance estimates due to interfering sidelobes of the resulting noncausal components of the radar echo [2]. However, since the error decreases with increasing bandwidth, it is negligible for ranging with UWB mmWave radar.

III. Free-Space Path

A. Refractive Index of Moist Air at mmWave Frequencies

Electromagnetic (EM) waves propagating through the atmosphere are affected by molecular gaseous absorption, where the main absorbers are oxygen and water vapor [26] causing attenuation [see Fig. 2(a)] and delay. On a macroscopic scale, this effect is described by the refractive index,

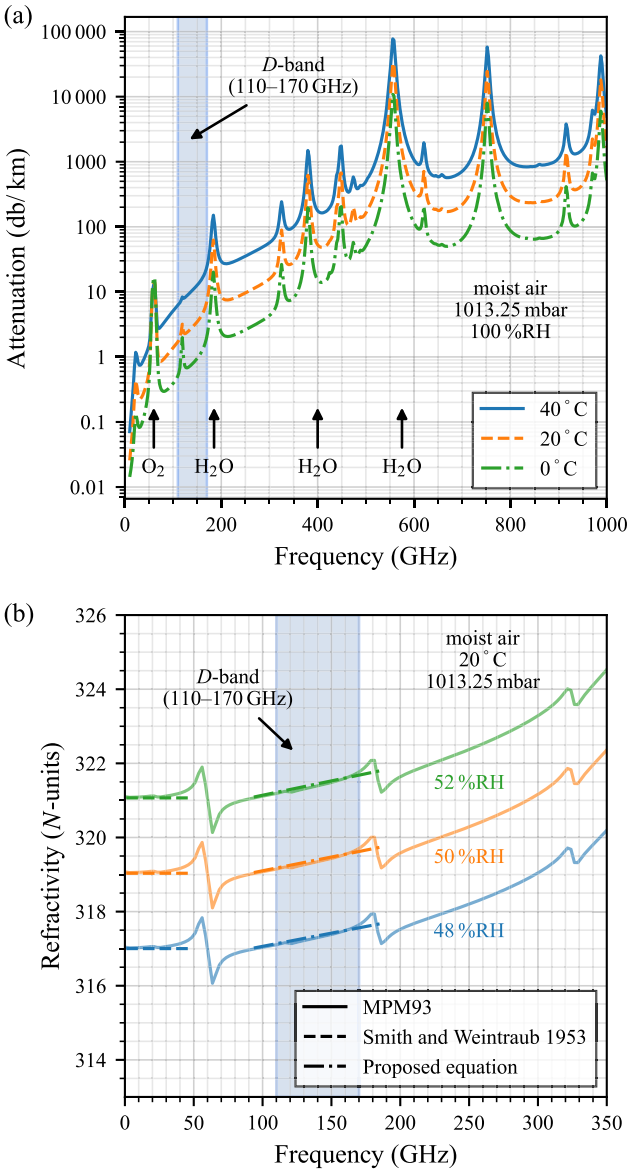

Fig. 2. Simulated (a) attenuation and (b) refractive index of moist air.

where the imaginary component refers to the attenuation, and the real component is the factor by which the wave is slowed down relative to vacuum. Using monostatic radar, the following relation between the measured distance r and the ToF τ applies:

$$r = \frac{\tau}{2}\frac{c_0}{n} \tag{7}$$

where c_0 is the speed of light in vacuum, and n is the real refractive index, commonly referred to as the refractive index. Whereas estimates of the real refractive index in accurate long-range distance measurements via radio waves are taken into account [27], in short-range radar application, the refractive index of air is usually neglected. Thus the propagation speed of the EM waves is assumed to be constant, for example, the speed of light in vacuum. This even applies to applications, where the authors are claiming very high accuracy [2]–[10] since the measuring range, there are just

millimeters to centimeters. However, if the measuring range exceeds the scale of multiple meters, errors of up to several hundred parts per million (ppm) become significant. This also applies if the measuring range is small but the initial distance is large (see also "dead path error" [28]).

A most commonly used model of the atmospheric refractive index at microwave frequencies up to 1000 GHz [29], [30] is the 1993 version of Liebe's Millimeter-Wave Propagation Model [31] (henceforth called MPM93). MPM93 works on the principle of line-by-line summation of oxygen and water vapor spectra. It considers contributions of 44 oxygen and 30 local water lines. An additional empirical continuum supported by many laboratory measurements accounts for far-wing contributions and improves the overall performance. The dry air and the water vapor module of MPM93 use frequency, ambient temperature, and the partial pressures of dry air and water vapor as input. Moreover, MPM93 provides modules for cloud/fog effects and Zeemann-broadening under mesospheric conditions, which have all been ignored here.

For the sake of computational complexity, it is valuable to have a simple closed-form expression for the computation of the radio refractive index, which can be efficiently computed on embedded devices. Numerous equations were reviewed in [27]. A commonly used [32] three-term expression was formulated by Smith and Weintraub [33] in 1953

$$N = (n-1)\,10^6 = K_1 \frac{p_\mathrm{d}}{\vartheta} + K_2 \frac{p_\mathrm{w}}{\vartheta} + K_3 \frac{p_\mathrm{w}}{\vartheta^2} \tag{8}$$

where N is the refractivity which is a common definition to characterize the refractive index of atmosphere in ppm, ϑ is the absolute temperature, p_d is the partial pressure of dry air, and p_w is the partial pressure of water vapor. The coefficients K_1–K_3 are

$$\begin{aligned} K_1 &= 77.6\ \mathrm{K\,mbar^{-1}} \\ K_2 &= 72\ \mathrm{K\,mbar^{-1}} \\ K_3 &= 375 \cdot 10^3\ \mathrm{K^2\,mbar^{-1}} \end{aligned}$$

where the K_1 and K_2 terms account for the concentration of dry gas and water vapor molecules, respectively. The additional K_3 term is due to the polarity of water molecules.

Different from outdoors, the concentration of carbon dioxide indoors, for example, in the laboratory, can vary considerably, leading to a significant deviation of the radio refractive index. Following [27], the three-term expression can be extended by an additional K_4 term [34] that takes the radio refractive index due to a variation of the carbon dioxide concentration into account:

$$N_\mathrm{c} = K_4 \frac{p_\mathrm{c}}{\vartheta}, \quad \text{with } K_4 = 133.5\ \mathrm{K\,mbar^{-1}}. \tag{9}$$

Here, p_c is the partial pressure of carbon dioxide. From (9), it can be noted that an increasing carbon dioxide concentration of 3000 ppm increases the refractive index by about 1.4 ppm under standard conditions.

As can be seen in Fig. 2(b), the equation proposed by Smith and Weintraub (8) is appropriate for frequencies up to 30 GHz. But for higher microwave frequencies, moist air is dispersive, thus, the three-term and four-term expressions become increasingly inaccurate. To account for wings of strong water lines, we propose an additional K_5-term

$$N_f = K_5 \frac{p_\mathrm{w}}{\vartheta} f \tag{10}$$

which is a linear function of frequency f. Finally, we obtain a new five-term expression

$$N = K_1' \frac{p_\mathrm{d}'}{\vartheta} + K_2 \frac{p_\mathrm{w}}{\vartheta} + K_3 \frac{p_\mathrm{w}}{\vartheta^2} + K_4 \frac{p_\mathrm{c}}{\vartheta} + K_5 \frac{p_\mathrm{w}}{\vartheta} f \tag{11}$$

which approximates the refractive index in the D-band ranging from 110 to 170 GHz. In (11), p_d' is the partial pressure of dry carbon dioxide-free air. The parameters K_1', K_2, K_3, and K_5 were obtained by fitting on the MPM93 data in a certain range of atmospheric conditions (0–50 °C, 900–1100 mbar, 0–100%RH) as

$$\begin{aligned} K_1' &= 77.56\ \mathrm{K\,mbar^{-1}} \\ K_2 &= 36.56\ \mathrm{K\,mbar^{-1}} \\ K_3 &= 381 \cdot 10^3\ \mathrm{K^2\,mbar^{-1}} \\ K_4 &= 133.5\ \mathrm{K\,mbar^{-1}} \\ K_5 &= 186.2 \cdot 10^{-3}\ \mathrm{K\,mbar^{-1}\,GHz^{-1}} \end{aligned}$$

where we assumed 300 ppm as a historic concentration of carbon dioxide.

The proposed equation (11) agrees very well with the MPM93 simulations [see Fig. 2(b)]; the difference in the refractive indices is at most 0.49 ppm. However, the radar system used in this work exceeds the D-band by 12 GHz. Nevertheless, the mean error over the radar's frequency range is at most only 0.25 ppm, whereas it would be 4.29 ppm using the equation formulated by Smith and Weintraub (8). These two values serve as measures of maximum ranging error due to the respective level of approximation made in (11) and (8).

It should be noted that, unlike optical metrology, relative humidity is the most critical parameter of moist air at microwave frequencies. For instance, at standard conditions (20 °C, 1013.25 mbar), an increase in relative humidity from 50% to 51% changes the refractive index by 1.03 ppm at 154 GHz, whereas it changes only by 0.01 ppm at a wavelength of 633 nm [35].

B. Systematic Error Introduced by Far-Field Assumption

In optical range-finding, for example, Michelson interferometry, the wavelength is usually negligibly small relative to the dimensions of the lenses and the mirrors. Moreover, the beam waist is always small compared to the mirror's diameter leading to specular reflection. This is fundamentally different from radar metrology, where one often assumes far-field conditions: point source of radiation (antenna phase center), point scatterer (target scattering center), and plane waves. However, far-field assumptions are imperfect because the antenna aperture and the target cross section are not point-shaped. They are inhomogeneously illuminated, and the wavefronts are curved (see Fig. 3). The radar target appears at a greater distance than the straight-line distance from the radar to the target. The systematic error is up to a quarter of the mean wavelength (here: 487 μm), and it is a function of frequency, orientation,

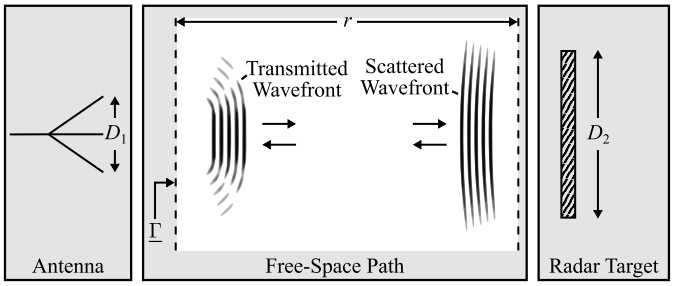

Fig. 3. Schematic of propagating waves on the free-space path to illustrate the error introduced by far-field assumption.

and distance. We propose two models for near-field correction: a simulation model and an approximate model. Interested readers might refer to [25], where the underlying theory is derived in detail.

1) Simulation Model: The fields and the waves are expressed in the frequency domain using a one-port network formulation for the radar path. Under far-field conditions (i.e., plane wave propagation in free space) the reflection coefficient of a system with a single reflection is

$$\underline{\Gamma}_{\mathrm{ff}} = -\frac{G\lambda}{|\boldsymbol{r}|^2}\sqrt{\frac{\sigma}{(4\pi)^3}}\exp(-\mathrm{j}k2|\boldsymbol{r}|) \tag{12}$$

where G is the antenna gain, λ is the wavelength, k is the angular wavenumber, $\boldsymbol{r}$ is the relative position of the target scattering center with respect to the antenna phase center, and σ is the target's radar cross section (RCS). Without far-field approximation, a more accurate solution is obtained by integrating the electric fields over a surface S bounding the antenna aperture

$$\underline{\Gamma} = -\frac{\iint_S \underline{\boldsymbol{E}}^+(\boldsymbol{r}')\cdot\underline{\boldsymbol{E}}^-(\boldsymbol{r}')\,\mathrm{d}s}{\iint_S \underline{\boldsymbol{E}}^+(\boldsymbol{r}')\cdot\underline{\boldsymbol{E}}^+(\boldsymbol{r}')\,\mathrm{d}s}. \tag{13}$$

Here, $\underline{\boldsymbol{E}}^+(\boldsymbol{r}')$ and $\underline{\boldsymbol{E}}^-(\boldsymbol{r}')$ are the electric fields of the transmitted and incident waves which are obtained by full-wave EM simulation and by the methods of physical optics, respectively. The phase response of a system describing the radar path's phase variation with respect to far-field propagation of waves is computed by

$$\phi_{\mathrm{var}}^{f} = \arg\left(\frac{\underline{\Gamma}}{\underline{\Gamma}_{\mathrm{ff}}}\right). \tag{14}$$

As the phase response is in good approximation of generalized linear phase, it can be described by two parameters $\Delta\varphi$ and $\Delta\tau$ [see (5)]. Both parameters are obtained by the linear least-squares method as

$$[\Delta\varphi \quad \Delta\tau]^{\mathrm{T}} = (\mathbf{A}^{\mathrm{T}}\mathbf{A})^{-1}\mathbf{A}^{\mathrm{T}}\boldsymbol{y} \tag{15}$$

where

$$\boldsymbol{y} = \left[\phi_{\mathrm{var}}^{f_0} \quad \phi_{\mathrm{var}}^{f_1} \quad \ldots \quad \phi_{\mathrm{var}}^{f_{M-1}}\right]^{\mathrm{T}} \tag{16}$$

is a column vector of simulated phase variations, and

$$\mathbf{A} = \begin{bmatrix} 1 & 1 & \ldots & 1 \\ 2\pi(f_{\mathrm{ctr}}-f_0) & 2\pi(f_{\mathrm{ctr}}-f_1) & \ldots & 2\pi(f_{\mathrm{ctr}}-f_{M-1}) \end{bmatrix}^{\mathrm{T}} \tag{17}$$

is an M by two matrix whose entries refer to the respective frequency values.

2) Approximate Model: The approximate model is a scalar approximation that arises from the simulation model. Assuming a planar circularly symmetric antenna aperture and a planar circularly symmetric radar target with diameters of D_1 and D_2, respectively. Both surfaces are considered to be illuminated uniformly, and incident wavefronts are spherical and of constant amplitude. The radar target is perfectly aligned in the antenna boresight at a distance of r. Then, one can find the following expressions as an approximate model:

$$\Delta\varphi(r) = -\frac{\left[(D_1)^2+(D_2)^2\right]\pi f_{\mathrm{ctr}}}{4rc_0} \tag{18}$$

and

$$\Delta\tau(r) = \frac{(D_1)^2+(D_2)^2}{8rc_0}. \tag{19}$$

IV. Signal Processing

The baseband radar echo is given as

$$\underline{h}(t) = \underline{g}(t-\tau)\,\exp(\mathrm{j}\varphi) \tag{20}$$

where $\underline{g}(t)$ denotes the pulse shape, τ is the group delay, and $-\varphi/(2\pi f_{\mathrm{ctr}})$ is the phase delay at center frequency. Hereinafter, τ and φ are referred to as pulse position and pulse phase, respectively. Most commonly, standard resolution methods are used and the ToF is obtained from the pulse position. However, using the pulse phase is beneficial in terms of noise, interference, and micromotions [2], [14], [24], [36]–[38], but as the phase is ambiguous in general, it requires more sophisticated signal processing.

A block diagram of the proposed signal-processing chain is given in Fig. 4. First, the input signal $X = (X_0, \ldots, X_{I-1})$ is conditioned by means of an inverse filter $\underline{G}$, and a window function W

$$\underline{Y}_i = X_i\,\underline{G}_i\,W_i, \quad i = 0, 1, \ldots, I-1 \tag{21}$$

where the frequency is assigned to the respective sample i as

$$f_i = f_{\mathrm{ctr}} + \left(\frac{i}{I-1}-\frac{1}{2}\right)B. \tag{22}$$

Here, I is the number of samples per sweep, and B denotes the bandwidth. Equation (22) requires reversing the order of the input signal's samples for downchirps in advance. We used a Hann window, which is a good compromise between the mainlobe width and sidelobe level. The inverse filter is necessary to restore the altered pulse shape due to the frequency response of the transceiver. It also increases the signal-to-noise ratio (SNR). The filter is determined once during initialization through time-gating of the radar echo (see also [14], [24]).

As the IF data is sampled symmetrically around the center frequency, one should use a centered definition of the inverse fast Fourier transform (IFFT) or inverse discrete Fourier transform (IDFT) to obtain time-domain data. Virtually all implementations of FFT/IFFT and DFT/IDFT are

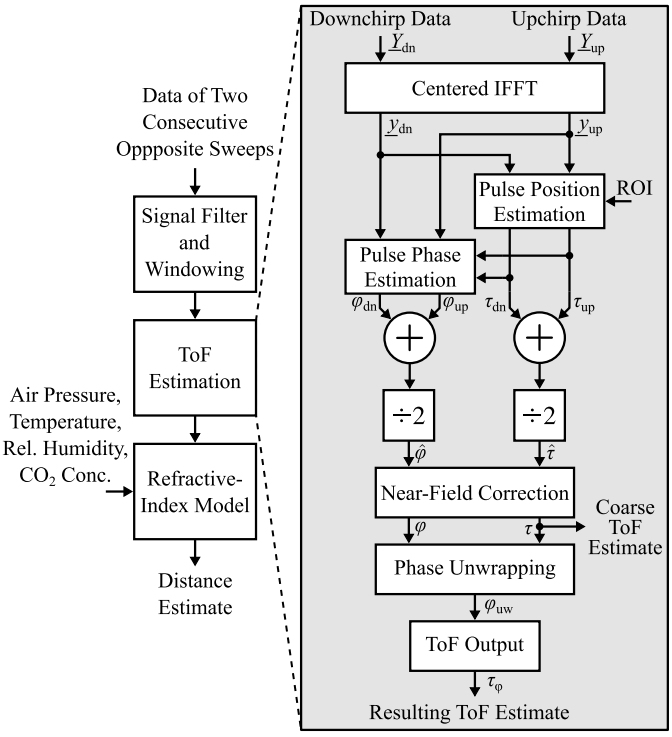

Fig. 4. Block diagram of the signal-processing chain.

noncentered [39], for example, in MATLAB, Mathematica, and Numpy. Therefore, the input data of the noncentered IFFT definition requires reorganization by means of a circular shift such that the first element of the input array refers to the center frequency. Since this procedure requires an odd number of samples, alternatively, the output data can also be multiplied by a phase term

$$\underline{y}_i = \mathrm{IFFT}\{(\underline{Y}_0, \underline{Y}_1, \ldots, \underline{Y}_{I-1})\}_i \exp\left(-\mathrm{j}\pi i \frac{I-1}{I}\right) \quad (23)$$

where the causal component of the time axis is

$$t_i = \frac{i}{B}\frac{I-1}{I}. \quad (24)$$

Centered IFFT processing only affects the phase response of the output data. The magnitude response remains unchanged. It is advantageous, as the random error of the pulse-phase estimate gets independent of the random error of the pulse-position estimate. This can be explained in an intuitive way by a "flat" phase response around the pulse peak (see also [40]).

Interpolation is used to refine the coarse estimate of the impulse response's peak location $\hat{i}$ obtained in a given region of interest (ROI). The interpolation procedure is based on a modified quadratic interpolation [14], [41], [42] using three samples nearest the peak

$$i = \hat{i} - \frac{|\underline{y}_{\hat{i}}|^p - |\underline{y}_{\hat{i}+1}|^p}{2|\underline{y}_{\hat{i}}|^p - |\underline{y}_{\hat{i}+1}|^p - |\underline{y}_{\hat{i}-1}|^p} + \frac{1}{2} \quad (25)$$

where the magnitude response is power-scaled with respect to the expected pulse shape thus the window function, via an optimized tuning parameter[2] p. The method is of low computational cost, it is highly accurate even at low SNR [42], and it is robust to interference [41]. Subsequently, the pulse phase is obtained at the interpolated peak location by using linear interpolation of the locally unwrapped phase response.

The time-domain estimates of two consecutive opposite measurements are arithmetically averaged

$$\hat{\tau} = \frac{\tau_{\mathrm{up}} + \tau_{\mathrm{dn}}}{2}, \quad \text{and } \hat{\varphi} = \frac{\varphi_{\mathrm{up}} + \varphi_{\mathrm{dn}}}{2} \quad (26)$$

in order to correct potential Doppler shifts, the phase response of the IF path (2), and the residual phase term (4) (see [14]). The effect of timing delays between the RF synthesizer and the ADC, which lead to an incorrect mapping between samples and frequencies, also cancels out provided the timing delays are symmetric for both sweep directions.

A near-field correction is applied

$$\tau = \hat{\tau} - \Delta\tau(r_{\hat{\tau}}), \quad \text{and } \varphi = \hat{\varphi} - \Delta\varphi(r_{\hat{\tau}}) \quad (27)$$

which compensates for the systematic error introduced by the far-field assumption. Here, $\Delta\tau(r)$ and $\Delta\varphi(r)$ are either precomputed lookup tables using the simulation model, or they are calculated on-the-fly using the approximate model (18), (19). The approximate measurement of distance $r_{\hat{\tau}}$ is obtained from $\hat{\tau}$. It should be noted that the effect of inaccurate estimates of $r_{\hat{\tau}}$ on the near-field correction is usually negligible.

Taking advantage of the unambiguous estimation of pulse position, a globally unwrapped phase value is obtained by [37]

$$\varphi_{\mathrm{uw}} = \varphi - \left\lfloor \frac{2\pi f_{\mathrm{ctr}}\tau + \varphi}{\pi} \right\rceil \pi \quad (28)$$

where $\lfloor\cdot\rceil$ denotes rounding to the nearest integer. The resulting ToF value based on the pulse phase is

$$\tau_\varphi = -\frac{\varphi_{\mathrm{uw}}}{2\pi f_{\mathrm{ctr}}} \quad (29)$$

which is then used to calculate the distance, by applying (7), where air temperature, pressure, humidity, and carbon dioxide readings are used as inputs to the proposed refractive-index model.

As the most computationally intensive part of the signal-processing chain is the IFFT of complexity $\mathcal{O}[I\ \log(I)]$ (see [39]), the computational complexity is low. Therefore, the computations can be made in real-time on cost-efficient embedded platforms.

V. Simulations and Experiments

A. Time-Domain Parameter Estimation

In order to characterize the signal-processing chain thus the proposed time-domain parameter estimators and to show whether additional estimation of the pulse phase is advantageous, we conducted a series of simulations using Monte Carlo methods. The estimators were analyzed in terms of noise, interfering reflections, and sinusoidal micromotions.

[2]Hann: $p = 0.23$, Hamming: $p = 0.19$, and Blackman: $p = 0.13$.

1) Noise: Fig. 5(a) shows the resulting root-mean-square error (RMSE) of simulated radar signals affected by additive white Gaussian noise at a given SNR. As can be seen, the random error using phase estimates is about ten times lower compared to only using estimates of pulse position. Moreover, at high SNR, pulse-position estimates are dominated by systematic uncertainties. The lowest value of RMSE is 450 nm. Cramér-Rao lower bound (CRLB) is used as a benchmark to evaluate the proposed estimators for random errors. Cramér-Rao gives a lower bound for the efficiency of an unbiased estimator: $\mathrm{CRLB}(\cdot) \leq \mathrm{Var}(\cdot)$. Following [14], [40], and [43], the CRLB using pulse position is

$$\mathrm{CRLB}(r_\tau) = \frac{3(c_0)^2}{2\eta_{\mathrm{snr}} I (2\pi B)^2} \tag{30}$$

and by using pulse-phase estimation it is

$$\mathrm{CRLB}(r_\varphi) = \frac{(c_0)^2}{8\eta_{\mathrm{snr}} I (2\pi f_{\mathrm{ctr}})^2} \tag{31}$$

where η_{snr} is the SNR in linear scale. From Fig. 5(a), one can see that the measures almost reach the CRLBs, thus the estimators are quasi-optimal in the sense of random errors.

2) Interfering Reflections: Fig. 5(b) depicts the maximum absolute error of estimates using simulations of radar signals in the presence of very close interfering reflections (clutter) with a certain signal-to-interference ratio (SIR). Like the RMSE in the noise case, the maximum absolute error for phase estimation is about ten times lower. As the range resolution scales linearly with the bandwidth, one can find the following relation for the maximum absolute error using pulse-position estimates by fitting on the simulated data:

$$\Delta r_\tau = \frac{0.3 c_0}{B\sqrt{\eta_{\mathrm{sir}}}}. \tag{32}$$

Here, η_{sir} is the SIR in linear scale. Following [14], the maximum absolute error using the pulse phase is

$$\Delta r_\varphi = \frac{c_0}{4\pi f_{\mathrm{ctr}}\sqrt{\eta_{\mathrm{sir}}}} \tag{33}$$

which unlike (32) depends on the center frequency rather than on bandwidth. The maximum error of the pulse-position estimate must not exceed $\pi/2$, so that the phase is unwrapped correctly. Therefore, using (32) the SIR threshold for correct phase unwrapping is

$$\eta_{\mathrm{sir,th}} = \left(\frac{2.4}{B_\%}\right)^2 \tag{34}$$

where $B_\%$ is the fractional bandwidth of the radar system. From (34), it can be concluded that a high fractional bandwidth is a key criterion for robust ToF estimation based on pulse-phase methods, which are required for micrometer accurate ranging. The radar system used has a particularly high fractional bandwidth of 36.4%, resulting in a minimum SIR of only 16.4 dB. By comparison, a usual short-range radar operating in the automotive band at 77–81 GHz would require an SIR of at least 33.5 dB, which is together with a lower center frequency and thus a lower antenna gain, only hard to achieve.

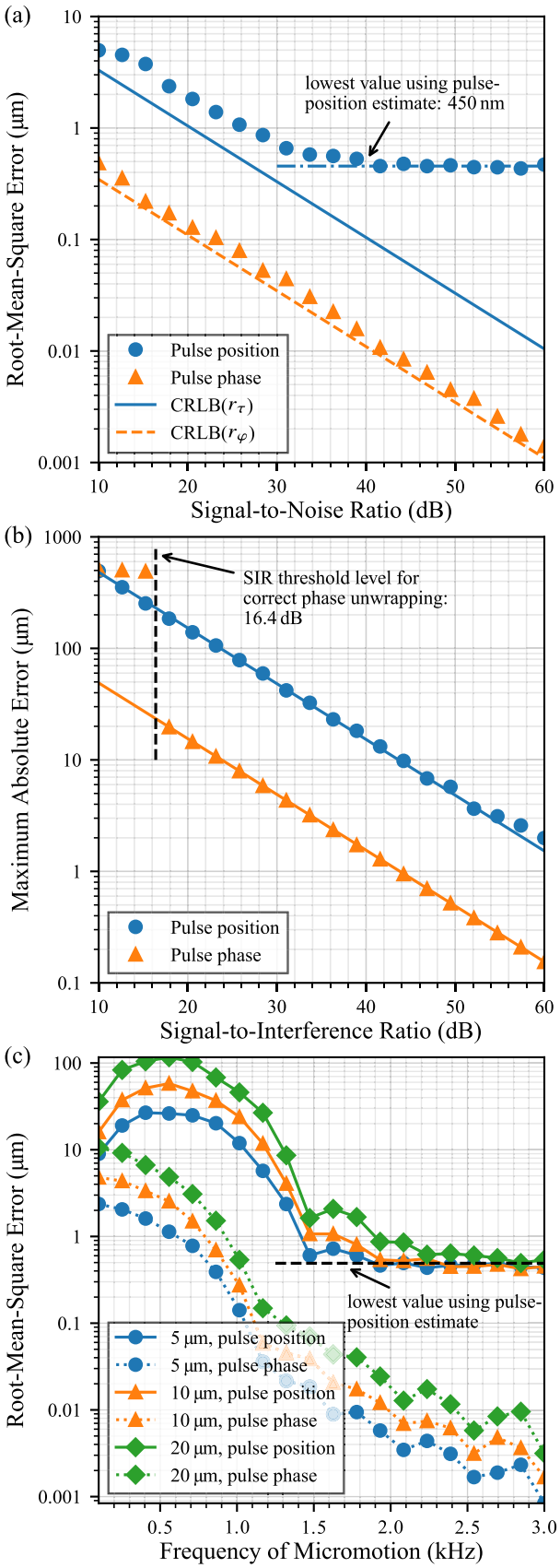

Fig. 5. Results of Monte-Carlo simulations to characterize the proposed parameter estimators in terms of (a) noise, (b) interfering reflections, and (c) sinusoidal micromotions of a given amplitude as labeled.

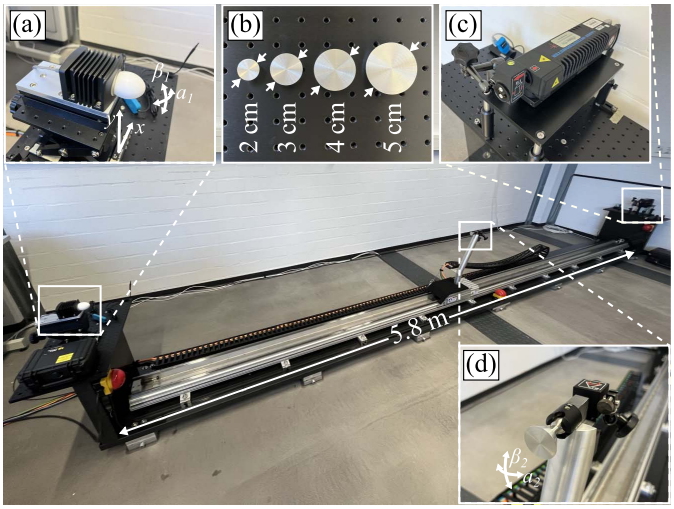

Fig. 6. Photograph of the experimental setup showing (a) radar sensor and environmental sensors, (b) variety of radar targets used, (c) laser measurement system, and (d) radar target and optical retro-reflector attached to the carriage of the linear rail.

3) Micromotions: A radar target in uniform motion causes a Doppler shift of the pulse position, which, however, cancels out by signal processing of two consecutive opposite sweeps. Whereas, sinusoidal micromotions cause a micro-Doppler, i.e., frequency modulation in the IF domain leading to interfering sidebands in the radar echo [37], which are described by Bessel functions of the first kind. In general, mechanical motions and radar samples are incoherent, therefore, a distorted pulse response leads to a random error in the parameter estimates. There are numerous reasons for unwanted micromotions which can degrade the precision of the measurement, for example, rotating or vibrating machines, or an active positioning control of the linear actuator. Fig. 5(c) shows the simulation results for the random error due to underlying micromotions with a respective amplitude of 5, 10, and 20 μm. It depicts the RMSE as a function of the micromotions' frequency. Especially the effect on distance estimates using pulse position is significant, as the random error is about 4–20 times higher compared to these using phase estimates. This again emphasizes the superiority of the proposed signal processing chain.

B. Laboratory Experiments

We conducted a series of experiments to evaluate the performance of the proposed measurement system regarding random errors, systematic errors, reproducibility, and scale errors. Fig. 6 shows a photograph of the experimental setup. A motorized linear guide with a travel range of at least 4.8 m was used for the positioning of a radar target. The radar system was placed on one end of the linear guide, whereas a laser measurement system was placed on the other end serving as a reference. The laser measurement system is based on a Michelson interferometer and has an accuracy of better than ± 0.4 μm/m. Instruments for accurate measurement of air temperature, relative humidity, air pressure, and carbon dioxide concentration were used. Their respective accuracies are at least ± 0.1 °C, ± 1.5%RH, ± 1.5 mbar, and ± 60 ppm. As listed in Table III, we used a set of small radar targets of circular shape, which have diameters of 2–5 cm, resulting in an RCS ranging from -4.9 to 11.1 dBsm. The respective SNR ranges from 13.5 to 25.9 dB at a distance of 5.1 m. Fig. 7 shows the resulting radar echoes using the smallest radar target of only 2 cm. Fig. 7 clearly reveals the r^{-4} far-field characteristic. Due to the high range resolution, the first reflection of the target is clearly distinguishable from reflections like antenna mismatch or multiple reflections. The very high gain of the antenna used, results in a pencil beam, thus, multipath propagation is negligible and there are no significant interfering reflections from surrounding scatterers providing sufficient SIR to achieve micron accuracy.

TABLE III
CHARACTERISTICS OF THE RADAR TARGETS USED

Diameter (mm)	20	30	40	50
RCS (dBsm)	−4.9	2.2	7.2	11.1
Measured SNR at 5.1 m (dB)	13.5	20.3	23.4	25.9

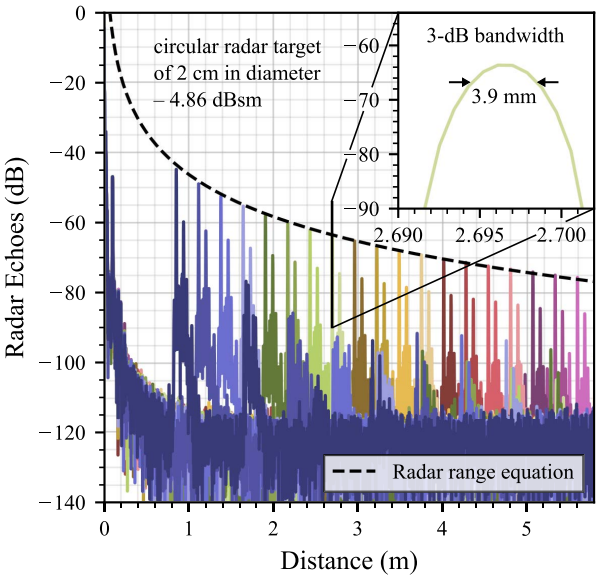

Fig. 7. Measured echoes of the smallest radar target with a diameter of 2 cm in the investigated range between 0.8 and 5.6 m.

1) Beam Alignment: In order to measure linear position highly accurate, beam alignment is required. The radar beam (i.e., the antenna boresight) should coincide with the linear path of the radar target. Misalignment causes a lower signal strength thus a lower SNR, and a second-order error also called cosine error [44]. This means that the distance appears larger than it actually is

$$\hat{r} = \sqrt{r^2 + \epsilon^2} \approx r + \frac{\epsilon^2}{2r}. \tag{35}$$

Here, ϵ is the displacement between the antenna and the linear path of the radar target. However, usually, the error term is negligible providing reasonable alignment. Unlike point scattering of radar targets in the far-field, specular reflections on a reflecting surface larger than the respective beam waist,

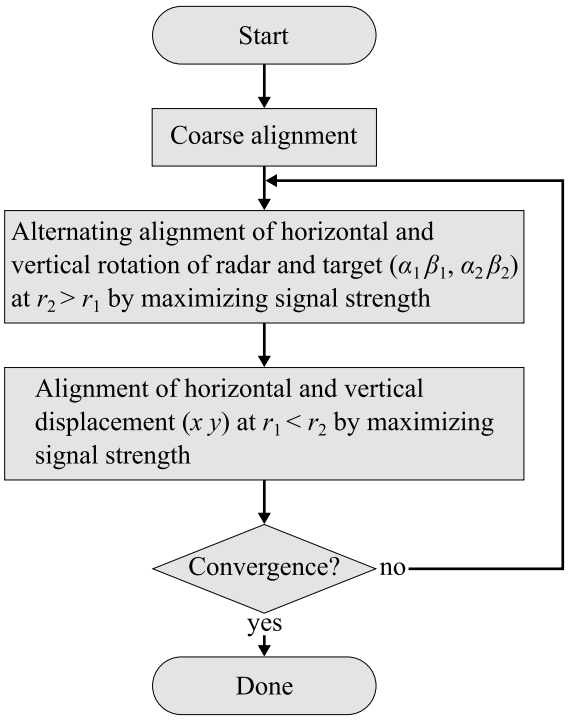

Fig. 8. Proposed beam alignment scheme for linear position measurement with planar radar targets.

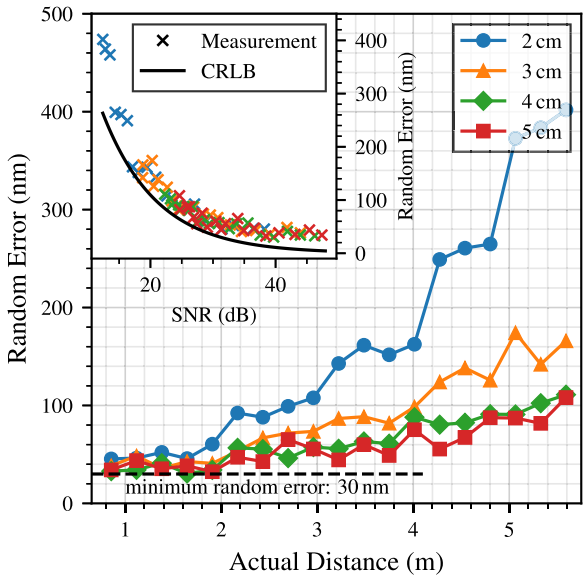

Fig. 9. Random errors quantified by the standard deviation of 100 consecutive measurements using circular radar targets of 2–5 cm.

that is if the radar target is very close to the antenna, cause a different type of cosine error

$$\hat{r} = 0.5\ r\,[1 + \cos(2\alpha)] \approx r\,(1 - \alpha^2) \tag{36}$$

which depends on the angle of incidence of the radar beam on the surface α.

As shown in Fig. 6(a), the radar system was attached on top of a lab platform consisting of a linear stage, a lab jack, and a pitch/yaw stage allowing horizontal and vertical displacement and rotation (x, y, and α_1, β_1, respectively). The respective radar target was attached to a ball mount [see Fig. 6(d)], allowing horizontal and vertical rotation of the target (α_2 and β_2). Fig. 8 depicts the scheme which we propose for beam alignment for planar radar targets. The procedure is based on iterative maximization of the received signal strength where the radar target is placed alternately at two different positions. The rotation is adjusted at the far position, whereas the displacement is adjusted at the near position. Usually, only a few iterations are required to achieve reasonable alignment.

2) Random Error: The random errors quantified by the standard deviation of 100 consecutive measurements are shown in Fig. 9 as a function of the actual radar-to-target distance. In addition, Fig. 9 shows the random error with respect to SNR estimates. At a distance of 5.6 m, the respective random error was about 400, 180, and 100 nm for the radar target of dimensions 2, 3, and 4 respective 5 cm. The curves of the two targets of highest RCS are coincident, and at distances greater than 2.5 m, they increase linearly with distance. This behavior can be explained by decorrelating phase noise, which dominated over additive noise at that range. The random error of every target decreased for shorter distances until it reached a minimum measurable value of about 30 nm. Usually, the quantization noise of the ADC determines the random error at shorter distances; however, here, the lower value is most probably due to small vibrations of the experimental setup.

3) Systematic Error: Fig. 10 shows the systematic errors of distance estimates referenced to the laser measurement system. Fig. 10 is divided into three subfigures, where (a) shows the distance errors without near-field correction, whereas in (b), the approximate model, and in (c), the simulation model was used. Without correction, the measured distance estimates varied up to 250 μm at a distance of 1 m, while it varied at a maximum of only 60 μm using the approximate model. With smaller targets and a greater propagation distance, the quality of far-field increases, and the estimates become more accurate. Using the target of 2 and 3 cm in diameter at a minimum distance of 1 m, the simulation model, in particular, stands out, as the error was better than ± 1 μm. Even with the approximate model, the residual error was fairly low. Consequently, depending on the accuracy requirements of the application, both models are appropriate for highly accurate ranging without sophisticated calibration of the distance value in advance. It should be noted that radar targets with a high RCS allow robust measurement with a low random error. However, a larger physical dimension of the radar target causes a greater bias, therefore it requires more near-field correction which is basically more prone to errors.

We conducted experiments to demonstrate reproducibility and to investigate scale errors under different atmospheric conditions. Highly accurate referenced distance measurements in air are only reliable under very stable conditions, as one must ensure a homogeneous atmosphere and no thermal expansion of the setup during the experiment. Therefore, the experiments were carried out on different days thus under different environmental conditions, without sophisticated air

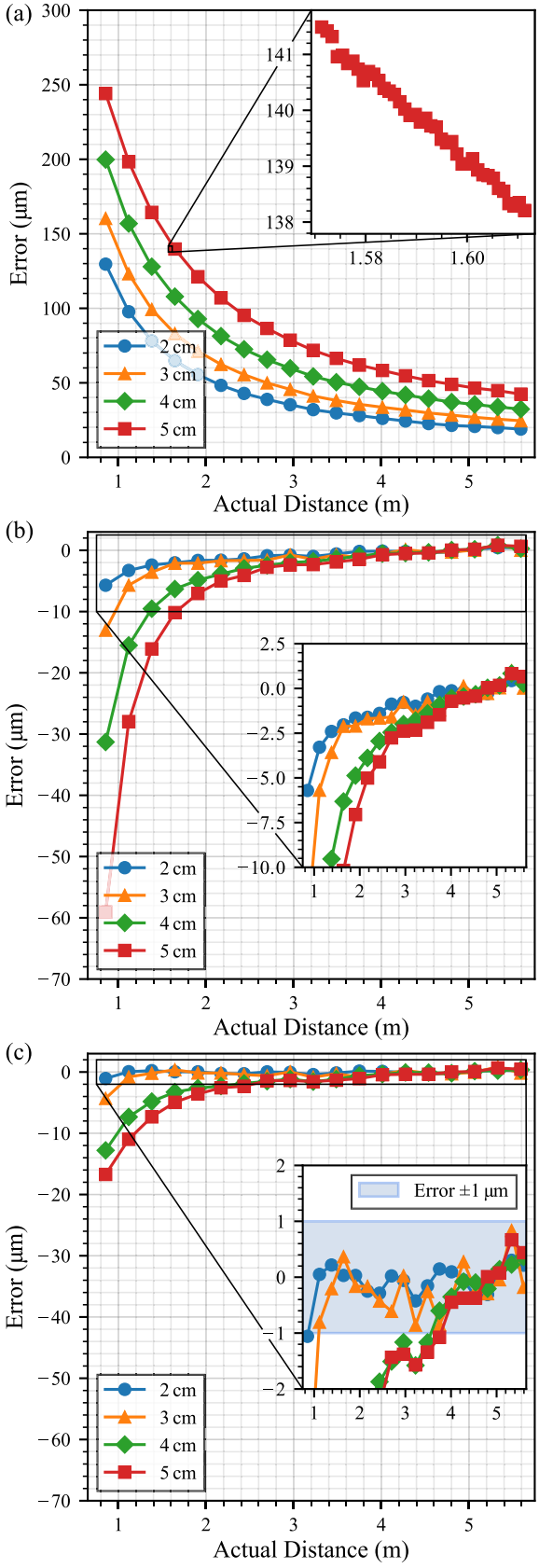

Fig. 10. Systematic errors of distance measurements using different models for near-field correction (a) not applied, (b) approximate model, and (c) simulation model. The line color indicates the radar target's diameter.

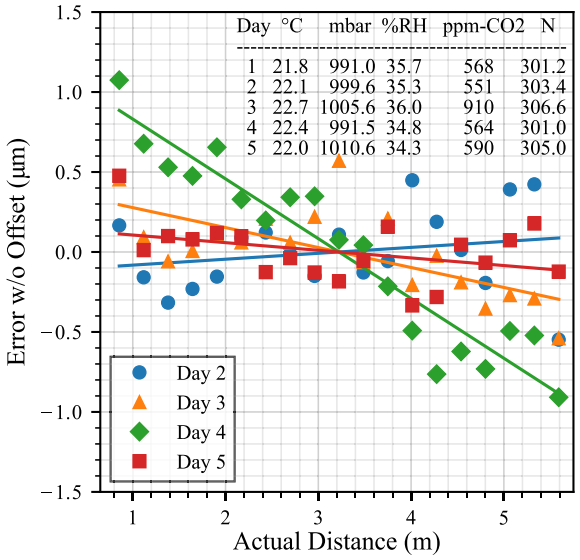

Fig. 11. Systematic errors of distance measurements of multiple experiments on one of five consecutive days, to demonstrate reproducibility and to investigate scale errors under different atmospheric conditions. The measured values of the first day were used as reference data. A circular radar target with a diameter of 3 cm was used.

conditioning. As the proposed equation for the refractive index of moist air is based on a proven model, there is no need for verification under a broad range of atmospheric conditions. Each measurement was conducted on one of five consecutive days, where the measured values of the first day were used as reference data. This experiment also serves as a benchmark if calibration is used. During the five days, the measured parameters of air were on average 22.2 °C, 999.7 mbar, 35.2%RH, and the carbon dioxide concentration was 637 ppm. The estimated refractivity ranged from 301.0 to 306.6, and thus the refractive index varied by 5.6 ppm. The measurement results are depicted in Fig. 11. Here, the radar target with a diameter of 3 cm was used. Fig. 11 reveals high reproducibility and very low scale errors. The resulting errors were in the range of ± 0.05 to ± 0.4 μm/m, which is lower than expected due to inaccurate humidity readings. The most accurate integrated humidity sensors[3] have a typical accuracy of ± 1 to ± 2%RH, which would lead to an error of ± 1.1 to ± 2.3 μm/m under the given conditions. Consequently, we achieved the maximum technologically feasible accuracy by compensation with modern environmental sensor technology.

VI. Conclusion

We have successfully demonstrated distance measurements with micrometer accuracy using a state-of-the-art FMCW radar. The radar system operates in the *D*-band, which enables sufficiently high bandwidth (range resolution), and a high antenna gain (directivity) despite a small antenna aperture (less near-field effects). We modeled the radar transceiver and the free-space path to apply near-field corrections and

[3]Sensirion's SHT series.

to compensate for the refractive index of air using an environmental sensor. The proposed signal-processing chain is robust to noise, interfering reflections, and micromotions. It is straightforward and of low computational cost such that it can be implemented on embedded platforms like the radar sensor itself. Without calibration of the distance value, experiments reveal a maximum error of only ± 1 μm over a measuring range of 4.8 m (0.8–5.6 m). The scale error obtained from multiple experiments on different days was less than ± 0.4 μm/m, and the random error was at least 30 nm, providing very high sensitivity. To the best of our knowledge, at present, these are the most accurate distance measurements using mmWave radar technology.

ACKNOWLEDGMENT

The authors would like to thank Status Pro Maschinenmesstechnik GmbH for the professional alignment of the linear guide setup.

REFERENCES

[1] G. Vinci, S. Lindner, F. Barbon, R. Weigel, and A. Koelpin, "Promise of a better position," *IEEE Microw. Mag.*, vol. 13, no. 7, pp. S41–S49, Nov. 2012.

[2] R. Stolle and B. Schiek, "Multiple-target frequency-modulated continuous-wave ranging by evaluation of the impulse response phase," *IEEE Trans. Instrum. Meas.*, vol. 46, no. 2, pp. 426–429, Apr. 1997.

[3] A. Stelzer, C. G. Diskus, K. Lubke, and H. W. Thim, "A microwave position sensor with submillimeter accuracy," *IEEE Trans. Microw. Theory Techn.*, vol. 47, no. 12, pp. 2621–2624, Dec. 1999.

[4] S. Lindner, F. Barbon, S. Mann, G. Vinci, R. Weigel, and A. Koelpin, "Dual tone approach for unambiguous six-port based interferometric distance measurements," in *IEEE MTT-S Int. Microw. Symp. Dig.*, Jun. 2013, pp. 1–4.

[5] T. Jaeschke, C. Bredendiek, S. Küppers, and N. Pohl, "High-precision D-band FMCW-radar sensor based on a wideband SiGe-transceiver MMIC," *IEEE Trans. Microw. Theory Techn.*, vol. 62, no. 12, pp. 3582–3597, Dec. 2014.

[6] S. Wibbing *et al.*, "A cost-efficient 61 GHz high-resolution radar sensor for industrial positioning and distance measurement," in *Proc. 21st Int. Conf. Microw., Radar Wireless Commun. (MIKON)*, May 2016, pp. 1–4.

[7] S. Scherr *et al.*, "Influence of radar targets on the accuracy of FMCW radar distance measurements," *IEEE Trans. Microw. Theory Techn.*, vol. 65, no. 10, pp. 3640–3647, Oct. 2017.

[8] M. Pauli *et al.*, "Miniaturized millimeter-wave radar sensor for high-accuracy applications," *IEEE Trans. Microw. Theory Techn.*, vol. 65, no. 5, pp. 1707–1715, Mar. 2017.

[9] S. Lindner, F. Lurz, S. Linz, R. Weigel, and A. Koelpin, "Mixer assisted interferometric six-port system for accurate distance measurements," in *Proc. Eur. Radar Conf. (EURAD)*, Oct. 2017, pp. 291–294.

[10] A. Bhutani, M. Pauli, T. Latzko, B. Gottel, M. Gehringer, and T. Zwick, "Micrometer-accuracy distance measurement using 122 GHz LTCC radar system-in-package," in *Proc. IEEE Asia–Pacific Microw. Conf. (APMC)*, Dec. 2019, pp. 753–755.

[11] N. Pohl *et al.*, "Radar measurements with micrometer accuracy and nanometer stability using an ultra-wideband 80 GHz radar system," in *Proc. IEEE Topical Conf. Wireless Sensors Sensor Netw. (WiSNet)*, Jan. 2013, pp. 31–33.

[12] T. Jaeschke, M. Vogt, C. Baer, C. Bredendiek, and N. Pohl, "Improvements in distance measurement and SAR-imaging applications by using ultra-high resolution mm-wave FMCW radar systems," in *IEEE MTT-S Int. Microw. Symp. Dig.*, Jun. 2012, pp. 1–3.

[13] S. Scherr *et al.*, "Miniaturized 122 GHz ISM band FMCW radar with micrometer accuracy," in *Proc. Eur. Radar Conf. (EuRAD)*, Sep. 2015, pp. 277–280.

[14] L. Piotrowsky, T. Jaeschke, S. Kueppers, J. Siska, and N. Pohl, "Enabling high accuracy distance measurements with FMCW radar sensors," *IEEE Trans. Microw. Theory Techn.*, vol. 67, no. 12, pp. 5360–5371, Dec. 2019.

[15] *UWB Radiodetermination Applications in the Frequency Range 116–260 GHz*, ECC Report 334, Copenhagen, Denmark, Jan. 2022.

[16] *Technical Characteristics, Exemption From Individual Licensing and Free Circulation and use of UWB Radiodetermination Applications in the Frequency Range 116–260 GHz*, Draft ECC Decision (22)03, Copenhagen, Denmark, Jun. 2022.

[17] *Spectrum Horizons*, FCC Rule, Washington, DC, USA, Jun. 2019.

[18] S. Kueppers, T. Jaeschke, N. Pohl, and J. Barowski, "Versatile 126–182 GHz UWB D-band FMCW radar for industrial and scientific applications," *IEEE Sensors Lett.*, vol. 6, no. 1, pp. 1–4, Jan. 2022.

[19] T. Jaeschke, S. Kueppers, N. Pohl, and J. Barowski, "Calibrated and frequency traceable D-band FMCW radar for VNA-like S-parameter measurements," in *Proc. IEEE Radio Wireless Symp. (RWS)*, Jan. 2022, pp. 64–67.

[20] N. Pohl, T. Jaeschke, and K. Aufinger, "An ultra-wideband 80 GHz FMCW radar system using a SiGe bipolar transceiver chip stabilized by a fractional-N PLL synthesizer," *IEEE Trans. Microw. Theory Techn.*, vol. 60, no. 3, pp. 757–765, Mar. 2012.

[21] K. Thurn, R. Ebelt, and M. Vossiek, "Noise in homodyne FMCW radar systems and its effects on ranging precision," in *IEEE MTT-S Int. Microw. Symp. Dig.*, Jun. 2013, pp. 1–3.

[22] S. Ayhan, S. Scherr, A. Bhutani, B. Fischbach, M. Pauli, and T. Zwick, "Impact of frequency ramp nonlinearity, phase noise, and SNR on FMCW radar accuracy," *IEEE Trans. Microw. Theory Techn.*, vol. 64, no. 10, pp. 3290–3301, Oct. 2016.

[23] N. Pohl and M. Gerding, "A dielectric lens-based antenna concept for high-precision industrial radar measurements at 24 GHz," in *Proc. 42nd Eur. Microw. Conf.*, Oct. 2012, pp. 405–408.

[24] B. Hattenhorst, L. Piotrowsky, N. Pohl, and T. Musch, "An mmWave sensor for real-time monitoring of gases based on real refractive index," *IEEE Trans. Microw. Theory Techn.*, vol. 69, no. 11, pp. 5033–5044, Nov. 2021.

[25] L. Piotrowsky, J. Barowski, and N. Pohl, "Near-field effects on micrometer accurate ranging with ultra-wideband mmWave radar," *IEEE Antennas Wireless Propag. Lett.*, vol. 21, no. 5, pp. 938–942, May 2022.

[26] J. Waters, *Methods in Experimental Physics* (Absorption and Emission by Atmospheric Gases), vol. 12. New York, NY, USA: Academic, 1976, pp. 142–176.

[27] J. M. Rüeger, "Refractive index formulae for radio waves," in *Proc. FIG 22nd Int. Congr. (ACSM-ASPRS)*, Apr. 2002.

[28] B. Dörband, H. Müller, and H. Gross, *Handbook of Optical Systems, Volume 5: Metrology of Optical Components and Systems* (Distance and Angle Metrology) Hoboken, NJ, USA: Wiley, 2012, pp. 489–558.

[29] D. D. Turner, M. P. Cadeddu, U. Lohnert, S. Crewell, and A. M. Vogelmann, "Modifications to the water vapor continuum in the microwave suggested by ground-based 150-GHz observations," *IEEE Trans. Geosci. Remote Sens. Lett.*, vol. 47, no. 10, pp. 3326–3337, Oct. 2009.

[30] P. W. Rosenkranz, "Water vapor microwave continuum absorption: A comparison of measurements and models," *Radio Sci.*, vol. 33, no. 4, pp. 919–928, Jul. 1998.

[31] H. J. Liebe, "Propagation modeling of moist air and suspended water/ice particles at frequencies below 1000 GHz," in *Proc. AGARD Meeting Atmospheric Propag. Effects Through Natural Man-Made Obscurants Visible MM-Wave Radiation*, May 1993.

[32] *The Radio Refractive Index: Its Formula and Refractivity Data*, document Rec. ITUR P.453-14, Aug. 2019.

[33] E. K. Smith and S. Weintraub, "The constants in the equation for atmospheric refractive index at radio frequencies," *Proc. Inst. Radio Eng.*, vol. 41, no. 8, pp. 1035–1037, Aug. 1953.

[34] A. C. Newell and R. C. Baird, "Absolute determination of refractive indices of gases at 47.7 gigahertz," *J. Appl. Phys.*, vol. 36, no. 12, pp. 3751–3759, Dec. 1965.

[35] P. E. Ciddor, "Refractive index of air: New equations for the visible and near infrared," *Appl. Opt.*, vol. 35, no. 9, p. 1566, Mar. 1996.

[36] L. Piotrowsky, T. Jaeschke, S. Kuppers, and N. Pohl, "An unambiguous phase-based algorithm for single-digit micron accuracy distance measurements using FMCW radar," in *IEEE MTT-S Int. Microw. Symp. Dig.*, Jun. 2019, pp. 552–555.

[37] L. Piotrowsky and N. Pohl, "Spatially resolved fast-time vibrometry using ultrawideband FMCW radar systems," *IEEE Trans. Microw. Theory Techn.*, vol. 69, no. 1, pp. 1082–1095, Jan. 2021.

[38] S. Scherr, S. Ayhan, B. Fischbach, A. Bhutani, M. Pauli, and T. Zwick, "An efficient frequency and phase estimation algorithm with CRB performance for FMCW radar applications," *IEEE Trans. Instrum. Meas.*, vol. 64, no. 7, pp. 1868–1875, Jul. 2015.

[39] W. L. Briggs and V. E. Henson, *The DFT: An Owner's Manual for the Discrete Fourier Transform* (Alternate Forms for the DFT). Philadelphia, PA, USA: Society for Industrial and Applied Mathematics, 1995, pp. 66–71.
[40] S. Schuster, S. Scheiblhofer, and A. Stelzer, "The influence of windowing on bias and variance of DFT-based frequency and phase estimation," *IEEE Trans. Instrum. Meas.*, vol. 58, no. 6, pp. 1975–1990, Jun. 2009.
[41] M. Gasior, "Improving frequency resolution of discrete spectra," Ph.D. dissertation, Dept. Elect. Eng., AGH Univ. Sci. Technol., Kraków, Poland, 2006.
[42] K. Werner and F. Germain, "Sinusoidal parameter estimation using quadratic interpolation around power-scaled magnitude spectrum peaks," *Appl. Sci.*, vol. 6, no. 10, p. 306, Oct. 2016.
[43] S. M. Kay, *Fundamentals of Statistical Signal Processing: Estimation Theory*. Upper Saddle River, NJ, USA: Prentice-Hall, 1993, pp. 27–81.
[44] S. D. Phillips, *Coordinate Measuring Machines and Systems* (Performance Evaluation). Boca Raton, FL, USA: CRC Press, 2012, pp. 183–272.

Lukas Piotrowsky (Graduate Student Member, IEEE) was born in Neuwied, Germany, in 1990. He received the B.Sc. degree from the Koblenz University of Applied Sciences, Koblenz, Germany, in 2016, and the M.Sc. degree in electrical and information engineering from Ruhr University Bochum, Bochum, Germany, in 2018.

Since 2018, he has been with the Institute of Integrated Systems, Ruhr University Bochum, where he is currently a Research Assistant. His research interests include system design of mmWave hardware and embedded signal processing.

Simon Kueppers (Graduate Student Member, IEEE) was born in Oberhausen, Germany, in 1988. He received the B.Eng. and M.S. degrees in electrical engineering from Ruhr University Bochum, Bochum, Germany, in 2008 and 2014, respectively, where he is currently pursuing the Ph.D. degree in millimeter-wave MIMO radar systems.

In 2015, he became a Researcher at the Fraunhofer Institute for High-Frequency Physics and Radar Techniques (FHR), Wachtberg, Germany, focusing on millimeter-wave MIMO radar systems. Since 2018, he has been the CTO of 2π-Labs GmbH, Bochum.

Timo Jaeschke (Member, IEEE) was born in Hattingen, Germany, in 1984. He received the Dipl.-Ing. and Dr.-Ing. degrees in electrical engineering from Ruhr University Bochum, Bochum, Germany, in 2011 and 2017, respectively.

From 2011 to 2018, he has been a Research Assistant with the Institute of Integrated Systems, Ruhr University Bochum. He is currently the CEO of 2π-Labs GmbH, a precision mmWave-Sensor company, Bochum. His current research interests include frequency synthesis, integrated ultrawideband frequency-modulated continuous-wave (FMCW) radar systems up to 240 GHz, high-resolution radar imaging, and highest precision distance and vibration measurements for various applications.

Dr. Jaeschke is a member of the Verband der Elektrotechnik, Elektronik und Informationstechnik (VDE), the Informationstechnische Gesellschaft (ITG), the European Microwave Association (EuMA), and the Deutsche Gesellschaft für Ortung und Navigation (DGON). He was a recipient of the IEEE Microwave Theory and Techniques Society (IEEE MTT-S) Graduate Fellowship Award in 2013 and the Airbus Defence and Space ARGUS Award in 2010. He was a co-recipient of the EuMIC Prize in 2012.

Nils Pohl (Senior Member, IEEE) received the Dipl.-Ing. and Dr.-Ing. degrees in electrical engineering from Ruhr University Bochum, Bochum, Germany, in 2005 and 2010, respectively.

From 2006 to 2011, he was a Research Assistant with Ruhr University Bochum, where he was involved in integrated circuits for mmWave radar applications. In 2011 and 2016, he became an Assistant Professor and a Full Professor of integrated systems, respectively, with Ruhr University Bochum. In 2013, he became the Head of the Department of mmWave Radar and High Frequency Sensors, Fraunhofer Institute for High Frequency Physics and Radar Techniques, Wachtberg, Germany. He has authored or coauthored more than 100 scientific articles and has issued several patents. His current research interests include ultrawideband mmWave radar, design and optimization of mmWave integrated SiGe circuits, and system concepts with frequencies up to 300 GHz and above, as well as frequency synthesis and antennas.

Dr. Pohl is a member of the Verband der Elektrotechnik, Elektronik und Informationstechnik (VDE), the Informationstechnische Gesellschaft (ITG), the European Microwave Association (EuMA), and the International Union of Radio Science (URSI). He was a co-recipient of the 2009 EEEfCom Innovation Award, the 2012 EuMIC Prize, and the 2015 Best Demo Award of the IEEE Radio Wireless Week and a recipient of the Karl-Arnold Award of the North Rhine-Westphalian Academy of Sciences, Humanities and the Arts in 2013 and the IEEE MTT Outstanding Young Engineer Award in 2018.